Chapter 2

Experimental Section: Materials Synthesis, Device Fabrication and Characterization Techniques

2.1 Introduction

To date, thin films of VO_2 can be deposited ($t \leq 100$ nm) on many substrates, using several methods, that include chemical-vapour deposition [1, 2], pulsed-laser deposition (PLD) [3–5], atomic layer deposition (ALD) [3, 6], magnetron sputtering [7, 8], molecular beam epitaxy [9, 10] and sol-gel method [11, 12] using various raw materials. Some of methods are describe in **Table 2.1** with their advantages, disadvantages and applications. Many are rather expensive processes and require sophisticated facilities and processing conditions in a controlled atmosphere. High-quality nano-architects (NAs) can be prepared of VO_2 type oxides of unified size, shape and topology by a simple hydrothermal reaction in a polymer solution [13–15], easier to scale up for large-scale applications. Therefore, in this thesis work utilized a well-known film-forming poly(vinyl pyrrolidone) (PVP) polymer [16–18], that leads to evenly dispersed $V^{5+} \rightarrow V^{4+}$ species on planar molecular PVP surfaces in nanocolloids that are easy to spin coat at a (100) Si substrate via a buffer SiO_2/TiO_2 layer. The buffer layer mediates to bond over VO_2 in a 2D network (nanoplates) via PVP along the VO_2-PVP films, which stays well stable on annealing (in optimized conditions) at VO_2 grows up uniaxial in (011) planes. Otherwise, VO_2 films often crack on anneals or/and are subjected to a field of operation in a device [19, 20]. The PVP protects a surface-stabilized VO_2 that stays well stable at long-term storage, or

heating safely up to its glass transition (T_g) ~ 457 K [21] in ambient air. Otherwise, a partial $V^{4+} \rightarrow V^{2+}$, V^{3+}, or V^{5+} conversion encounters fading its shelf life in a device. In this investigation, we developed a polymer PVP assisted M_1-VO_2 of thin films, $t \leq 100$ nm, with a nano SiO_2/TiO_2 gate on a (100) Si(p^{++}) substrate, using $V_2O_5 \rightarrow 2VO_2 + ½ O_2\uparrow$ finely dispersed via PVP in nanocolloids in hot water. Both SiO_2 and TiO_2 (as a template) support over a uniaxial (011) VO_2 growth in NCs primarily along the films.

Table 2.1 The different techniques for VO_2 thin film deposition.

Methods	**Ref.**
"Sol-Gel" **Advantages** • Straightforward and cost-effective. • Simple synthesis of homogeneous composites. • Capable of producing amorphous materials. • Possesses high chemical reactivity in precursors. **Disadvantages** • Prior familiarity with the gelling solution's composition is necessary. • The high moisture level necessitates post-deposition heat treatment. • The production of thicker films may result in shrinkage or cracking. • Involves extended preparation, aging, and curing times. **Applications** • The production of catalysts using wet chemical techniques, fabrication of thin films with intricate structures, doping processes, and production of composite oxide films.	[22–24]
"Atomic Layer Deposition (ALD)" **Advantages** • Inherent film quality is ensured by its self-limiting capability. • Capable of deposition on fragile substrates. • Produces incredibly thin films of superior quality with remarkable control over thickness and reproducibility.	[25–28]

• Makes it possible to apply several layers at once. **Disadvantages** • Significant energy wastage is implicated in the process. • The by-products can be highly toxic, necessitating meticulous management. • ALD incurs high costs, utilizing expensive precursors. • The reaction time of the chemicals involved in the process is time-consuming. **Applications** • Supercapacitors, power conversion, solar systems, and other energy-saving techniques.	
"Pulse Laser Deposition (PLD)" **Advantages** • Simple and customisable for the creation of homogenous and compatible films. • There are no restrictions on the range of PLD targets. • Environmentally friendly and simple to handle. **Disadvantages** • Film quality diminishes with the splashing of molten material. • PLD exhibits a slower deposition rate compared to alternative methods. • Inappropriate for deposition over large areas. • Vaporisation is the cause of material loss. **Applications** • PLD is most useful in fields like microelectronics, sensor technologies, optical manufacturing, and new material development.	[29–31]
"Spin Coating" **Advantages** • Cost-effective and straightforward to operate. • Rapid spin speeds facilitate prompt film drying. • Effortless overlay of various materials on distinct layers. • Simple adjustment of substrates and chemicals employed. **Disadvantages** • Processing only one substrate at a time. • The substrate size is limited by its holder.	[32–35]

• Not applicable for intricate shapes. • Involves high manufacturing waste. **Applications** • Fabrication in polymeric films, nano materials, SCs and ceramic products.	
"Sputtering" **Advantages** • Generates steady and reliable films. • Makes it easier for materials with a high melting point to deposit. • Capable of depositing a diverse range of materials. • Produces precise, excellent-quality films. **Disadvantages** • Certain materials necessitate extremely low deposition speeds. • The targeted area subjected to bombardment is limited in size. • Certain dielectrics require an RF energy source. • The equipment is intricate and entails high operational costs. **Applications** • SCs industries, flat panel displays, data storage and microelectronics.	[36–39]

2.2 Sol-gel Method

The sol-gel method is a versatile and widely employed technique for the synthesis of inorganic and hybrid materials, offering precise control over composition, structure, and morphology at the nanoscale. This process involves the transformation of a solution (sol) into a gel through the polymerization of precursor molecules, followed by a controlled drying process to form a solid material [40]. In this method, the sol undergoes a polycondensation process, transforming into an inorganic network with a liquid phase, referred to as gel. The expansion of the oxide network is influenced by self-assembly among the precursor molecules, involving covalent bonding, hydrogen bonding, and Van der Waals interactions [41]. This method is employed for the production of monoclinic

VO_2-based films, chosen for its simplicity in large-area deposition, cost-effectiveness, and practicality in seamlessly incorporating metal doping [42]. The pioneering work of Greenberg et al. in 1983 marked the inception of the sol-gel technique for depositing VO_2-based films, utilizing $VO(OC_3H_7)_3$ [43]. Subsequent research has revealed that an equivalent n-propoxide vanadium compound can be utilized to produce VO_2 using this method [43]. Employing spin coating, the precursor of VO_2 can be applied to a substrate (such as silicon, sapphire, aluminum, glass, etc.) to create a film based on VO_2. Following the drying phase and the formation of a porous material, a typical next step involves a calcination process. This process is usually undertaken to enhance the mechanical properties and crystallization of the VO_2 film.

2.3 Experimental Details

2.3.1 Materials

Highly pure (99.99 %) reagents V_2O_5, oxalic acid ($C_2H_2O_4 \cdot 2H_2O$) and PVP-K30 were used in a precursor of nanocolloids to make the VO_2@Si films. A buffer layer of SiO_2 and TiO_2, was used to regulate a (011) uniaxial VO_2 growth of NCs along the films. A pure and a SiO_2 coated (100) Si(p^{++}) were used as received from the Sigma Aldrich company. A buffer TiO_2 layer was made form an emulsion of titanium butoxide $Ti(C_4H_9O)_4$ by dissolving in 2-methoxy ethanol $C_3H_8O_2$ (from the Sigma Aldrich). To disperse V_2O_5 in H_2O via PVP to make $V_2O_5 \rightarrow 2VO_2 + ½O_2\uparrow$ in the form of a transparent hydrogel in order to spin coating it homogeneously in the films.

2.3.2 Synthesis of TiO_2 Buffer Layer

A sol-gel method is used to make a buffer layer TiO_2 as used earlier [13] and employed as a gate dielectric for metal oxide thin film memristors (TFMs). Accordingly, a 100-300

mM solution of $Ti(C_4H_9O)_4$ in 2-methoxy ethanol (stirred 1 h at 323 K) is spin-coated as a thin film on a cleaned (100) Si(p^{++}) substrate at a speed of 4000 rpm for 40 s, as used above to make the VO_2 films. A film TiO_2 is stabilized when dried at 373 K for 5 min in ambient air, subsequently subjected to an annealing process in an open atmosphere at 623 K for 30 minutes to decompose the precursor salt and form a thin film of TiO_2.

2.3.3 Synthesis of Thin VO_2 Films

The major steps used to make a polymer PVP assisted VO_2 of nanocolloids and films are summarized in the schematics in **Figure 2.1**.

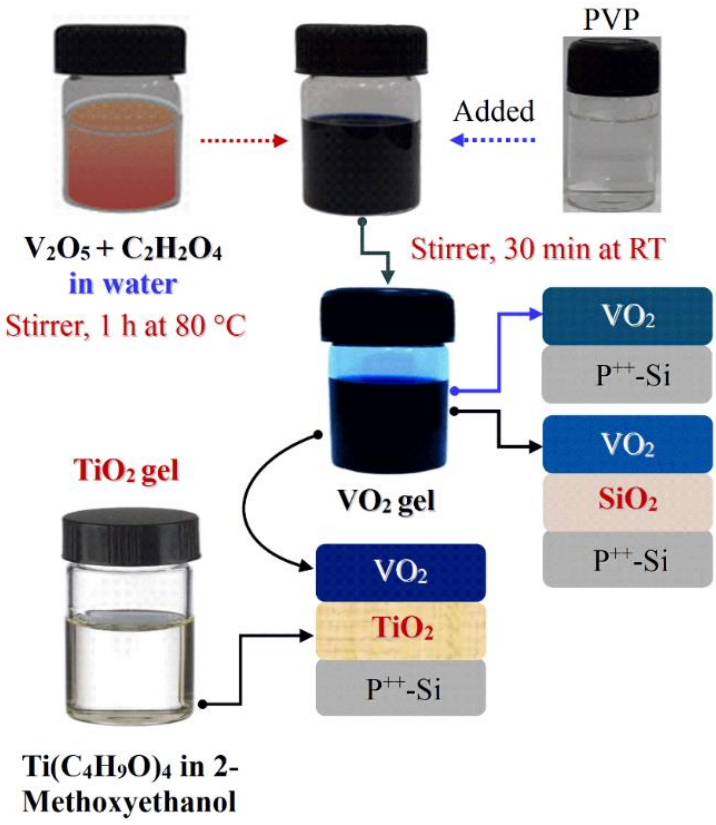

Figure 2.1 The experimental steps (schematics) used to reduce $V_2O_5 \rightarrow 2VO_2 + ½O_2 \uparrow$ in an aqueous acid followed by adding a polymer PVP to form a hydrogel suitable to spin coating (after heating at 353 K in the air) on pure and SiO_2/TiO_2 coated Si(p^{++}).

In a typical experiment, nanocolloids VO_2 were made from V_2O_5 (3.63 g) dispersed in $H_2C_2O_4{\cdot}2H_2O$ (a reducing agent) of 5.4 g in 30 mℓ water by stirring on a hot plate at ~ 353 K for 60 min, forming a homogenous sample. An aqueous PVP (0.2 gm in 10 mℓ water) solution was added by stirring 30 min at RT. A reddish-orange initial colour of the mixed solution is slowly turned up blackish and then a deep bluish in a due reaction, $V_2O_5 + 3H_2C_2O_4 \rightarrow 2VOC_2O_4 + 3H_2O + 2CO_2\uparrow$, incurs slowly over a time scale. The PVP bridges V^{4+} species in a polymer complex forming a hydrogel. At a planar PVP polymer, which serves as a template, a mineralizer, and a stabilizer [12, 44], a refined VO_2 in a thermal decomposition, $VOC_2O_4 + ½O_2\,(air) \rightarrow VO_2 + 2CO_2\uparrow$, adsorb and order in situ in VO_2 chains thereon led over its open surfaces. A filtered solution (passed through a micro-syringe (0.45 μm) to separate out from coagulates) was spin-coated onto pertinent substrates (preheated at 373 K) - a virgin and SiO_2/TiO_2 coated Si(p^{++}), using a spin coater at a 4000-rpm speed for 40 s. All three types of green VO_2 films made here on the three types surfaces are annealed for 3 h (in argon) at an optimized 823 K temperature to give rise to aligned (011) NCs of the M_1-VO_2 phase along the film surface.

2.3.4 Chemicals Bonding

In view of the observations, a nanogate inbuilt on the Si(p^{++}) regulates a chemical V-O bonding on and along it in order to form a 2D network VO_2 as follows. A way Si atom on the Si(p^{++}) can share the bonding to form a network of VO_6^{8-} octagons at V^{4+} sites via Si-O bonds along a permeable crystallographic [101] axis in a perpetual plane (011) VO_2 on the interface. Here, a-axis is setup perpendicular to the (011) plane as observed in the XRD pattern in a M_1-VO_2 lattice. A nanogate SiO_2, which contains tetrahedral units SiO_4^{4-}, forms a rather e-rich ‘O-Si-O-V-O’ oxo-bridging of a highly regaled network along the [101] axis. The (011) plane VO_2 is favoured to bonding up easily along the

interface at closely compatible octahedral units TiO_6^{8-} at n-TiO_2, as it is well reflected in the XRD pattern. An inbuilt gate n-TiO_2 serves as an 'electron donor' of tailoring the exotic electronic properties.

2.3.5 Fabrication of TFMs

Top-contact TFMs were fabricated on a highly doped silicon (100) Si(p^{++}) substrate in all of work. To make such devices, Si(p^{++}) wafers (15 mm x15 mm) were first washed in a soap solution and then cleaned via. water, acetone, and iso-propanol for 30 minutes respectively inside an ultra-sonication bath. After wet cleaning, the wafers were dried with dry air. Finally, all of the substrates were cleaned with oxygen plasma to make them hydrophilic, which is an important step before sol-gel thin film deposition, as it allows for excellent homogeneity of the thin film.

After dry cleaning, precursor solution of gate dielectric was spin-coated on cleaned Si(p^{++}) for 40 seconds at 4000 rpm in ambient air. To remove the solvent from the film, the spin-coated samples were placed on a pre-heated hot plate at 373 K for five minutes. After drying, the samples were annealed in a furnace for appropriate time and temperature. With the same technique, we coat the SC on top of the gate dielectric and finally, the metal electrodes were deposited by a thermal evaporator which will work as a source and drain. The following flow diagram in **Figure 2.2** shows the different steps used for TFMs fabrication.

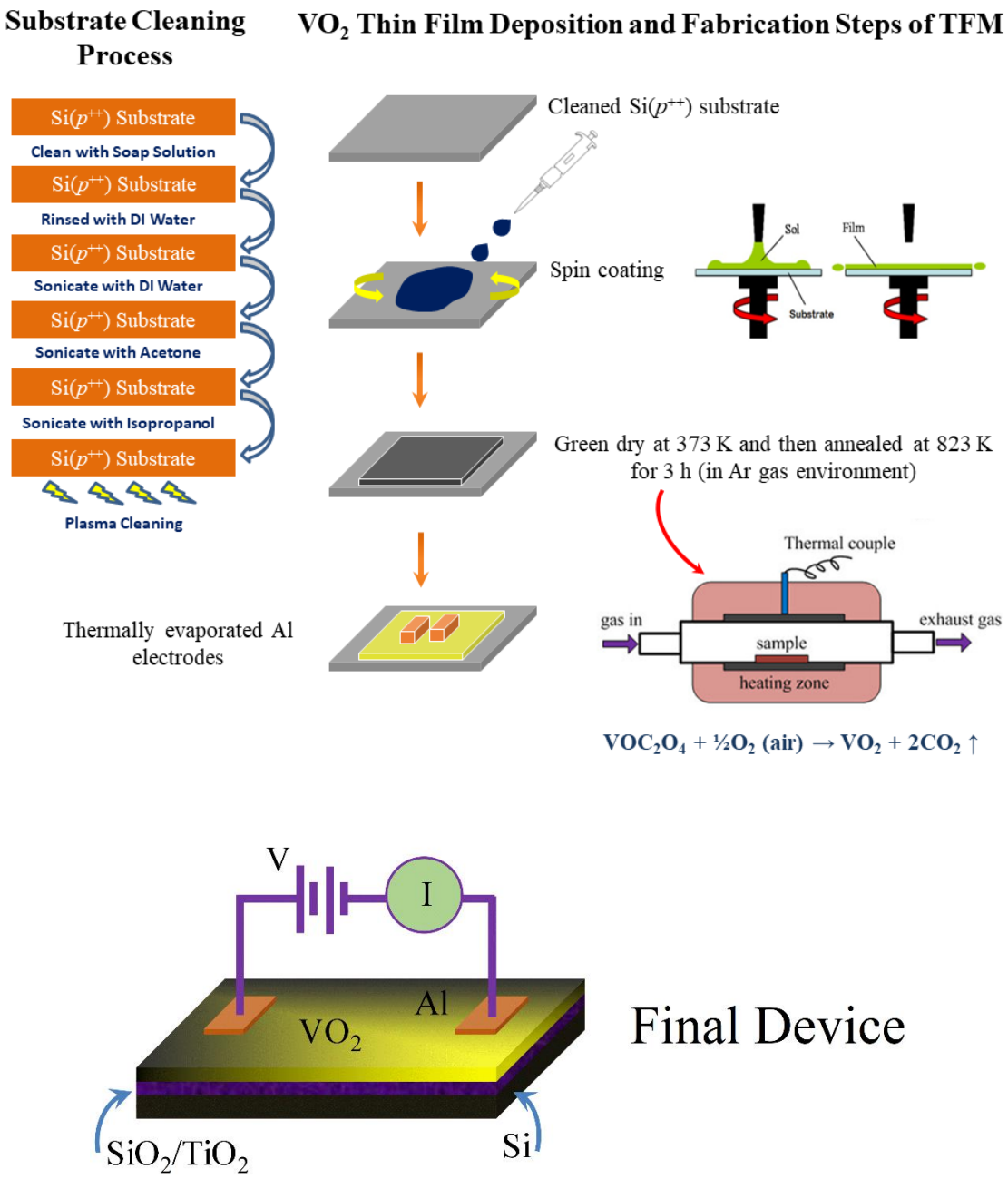

Figure 2.2 The cleaning and fabrication steps (schematics) used to deposit VO_2 thin film form a hydrogel suitable through spin coating on pure and SiO_2/TiO_2 coated Si(p^{++}) (Bottom panel shows the final device structure of TFMs).

2.4 Material Characterization

The XRD patterns, atomic force microscopy (AFM), field-emission scanning electron microscopy (FESEM), and high-resolution transmission electron microscopy (HRTEM) were used to characterise the VO_2 films consisting of small and coplanar VO_2 islands (nanoplates). The XRD patterns were measured in a range 10-90° of diffraction angle (2θ), using a Panalytical X'Pert Pro-diffractometer, with a filtered Cu-K_α radiation of λ = 0.15406 nm wavelength. The AFM images are studied using the Bruker IR3 AFM device. The FESEM images were recorded using a ZEISS EVO 60 FESEM at 10 to 20 kV acceleration voltage. An average t ~ 100 nm was estimated from the FESEM images at cross-sections of the films. A JEOL JEM-2100 HRTEM, operated at 200 kV, was used to study the shape, size, interfaces and surface topology of VO_2 NAs in the films. The Raman bands were measured in a backscattering configuration using a Horiba LABRAM-HR spectrophotometer, with a He-Ne laser (λ = 632.8 nm) used to excite the phonons in the films, as used earlier [45]. The laser beam was focused on a small spot (≤ 1 μm diameter) at the films to resolve closely spaced bands. Further, the V^{4+} (which involves an ion exchange to V^{5+} valent states) and O^{2-} species were analysed with XPS bands using an X-ray photoelectron spectrophotometer (XPS), Φ-ULVAC-PHI Inc, JAPAN (PHI 5000VERSA probe II), with an excitation source of 1486.6 eV Al-K_α radiation. The band positions were calibrated using the C-1 s band at 284.50 eV as a reference. Other details are the same as described elsewhere [46, 47]. A four-point probe method was used to measure the resistivity of the fabricated film. The scattering-type scanning near-field optical microscopy (s-SNOM) images are mapped at selected temperatures (across the T_c point) at the VO_2 films, using s-SNOM (Neaspec, GmbH) equipped with a near-field illumination (1 mW power) at an AFM tip (oscillating at a Mid-IR resonance frequency)

by a Mid-IR λ = 10.632 μm quantum cascade laser (QCL) (the Daylight Inc.). A home-built set-up with a small heater has been attached to the sample holder in order to vary and measure the temperatures (290 K to 400 K) at the films. The basic principle of a typical s-SNOM used in situ mapping the phase order at a nanoscale is described elsewhere [48–51]. The electrical properties are studied at 303 K to 473 K temperatures at 10^2 Hz to 10^6 Hz frequencies using a LCR meter called impedance spectroscopy (IS) [44, 52]. The I-V characteristics were measured at circular Al-electrodes pivoted at the films with the help of a thermal evaporator. The fields-witching was studied at two-probe geometry, with an electric field applied in steps of selective voltages, at an ON/OFF scheme. It allowed scanning the I-V characteristics at varied 0 → 30 V sweeping fields, using a specific SC device analyzer (KEYSIGHT B1500 A).

2.4.1 X-ray Diffraction

XRD serves as a powerful technique for the in-depth characterization of crystalline materials, providing crucial information about grain size, relative crystalline orientation, and lattice parameters [53]. In a crystalline structure, atomic planes are separated by a characteristic distance, denoted as d_{hkl}, and the identification of these lattice planes is facilitated through Miller indices h, k, and l. The intriguing aspect of XRD lies in the constructive interference of X-rays scattered from these atomic planes, resulting in the emergence of distinct diffraction peaks at specific angles [53].

This phenomenon is precisely described by Bragg's Law:

$$n\lambda = 2d_{hkl}\cdot\sin\theta$$

In this equation, λ represents the wavelength of incoming X-rays, θ denotes the scattering angle, and y is an integer indicating the order of the diffraction peak.

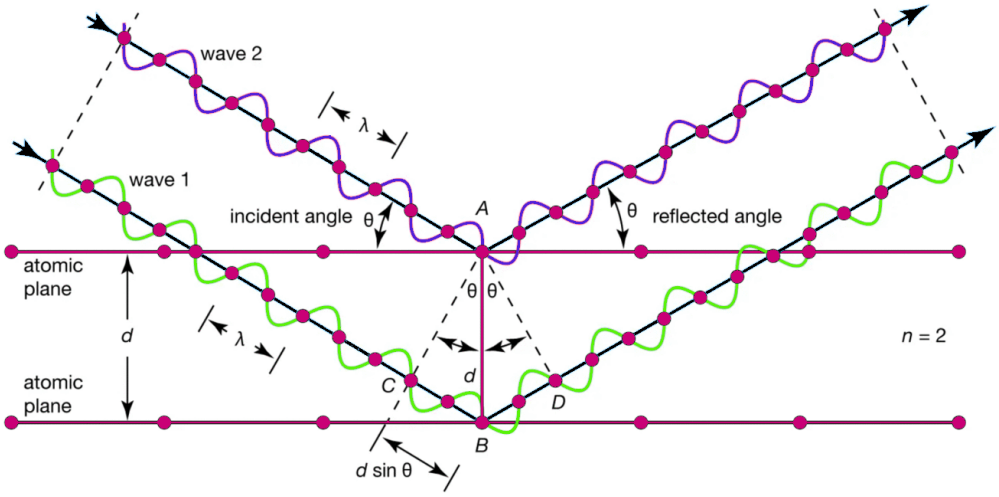

Figure 2.3 A graphical representation of Bragg's law equation.

This mathematical formulation elegantly captures the essence of XRD and its application in probing the crystalline structure of materials. For a more vivid understanding, consider **Figure 2.3**, where a graphical representation of Bragg's Law is depicted. The illustration showcases the interaction of X-rays with crystalline planes, the resulting diffraction pattern, and the significance of the scattering angle in determining diffraction peak positions. The peaks correspond to specific orders (n) and provide crucial insights into the internal arrangement of atoms in the material.

Now, let's delve into the study of thin films using the grazing incidence X-ray diffraction (GIXRD) technique. By employing a low incoming angle of incidence X-rays, GIXRD enhances sensitivity to thin film diffraction while minimizing unwanted substrate scattering [53]. This configuration enables researchers to precisely analyse the structural characteristics of thin films, unveiling valuable information about their crystallographic properties.

2.4.2 Atomic Force Microscopy

Surface morphology can be observed with SEM, but the insulator has to be coated with gold to have better contrast. AFM is a better technique to probe the surface morphology of the thin films in 3D utilizing the van der Waal forces between the tip and the sample surface [54]. AFM works on the van der Waal forces between the tip material and the sample surface, which is maintained with the feedback loop to record the nanoscale scanning (**Figure 2.4**). The forces can be repulsive or attractive based on the distance between the tip and the surface. If the distance is of few angstroms, it is repulsive and the AFM mode is known as "in contact," and if it is further from the surface, there will be an attractive force, and the AFM mode will be known as the "non-contact mode."

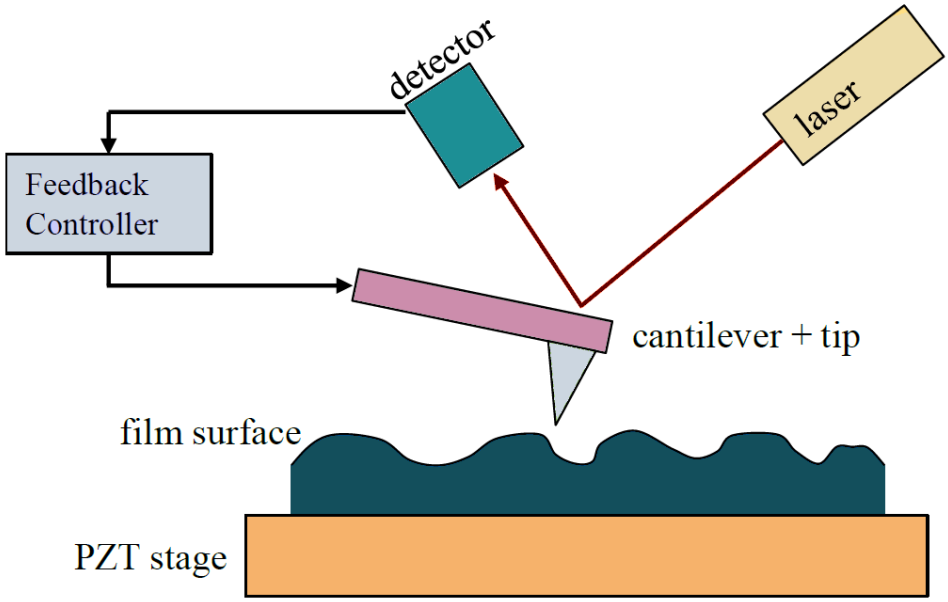

Figure 2.4 Schematic diagram of a typical AFM setup.

Usually, AFM is used in the tapping mode when the tip is oscillated at the resonance frequency and from a specific distance from the sample surface [54]. The essential factor

we can resolve from the AFM is surface roughness. The root mean square (rms) roughness is used most of the time. The rms roughness determines the root mean of the deviation of the surface elevation from the mean roughness.

2.4.3 Field-Emission Scanning Electron Microscopy

FESEM is a powerful tool employed to examine the surface morphology of samples. The process involves generating an electron beam in the electron gun, which passes through a series of lenses and apertures, resulting in the creation of a focused electron beam. This focused electron beam interacts with the atoms of the sample, producing various types of signals. Detectors are utilized to capture signals emanating from secondary electrons or backscattered electrons [55], which are employed for imaging purposes. The signals obtained from secondary electrons provide detailed insights into the surface structure of the sample, while signals from backscattered electrons offer valuable information regarding compositional contrast within the sample [55]. Furthermore, an energy dispersive X-ray analysis (EDX) system is integrated into the electron microscopy instrument. This system serves the dual purpose of offering both qualitative and quantitative chemical information about the analysed sample [55]. To provide a visual understanding, refer to **Figure 2.5**, illustrating the key components and processes involved in FESEM analysis.

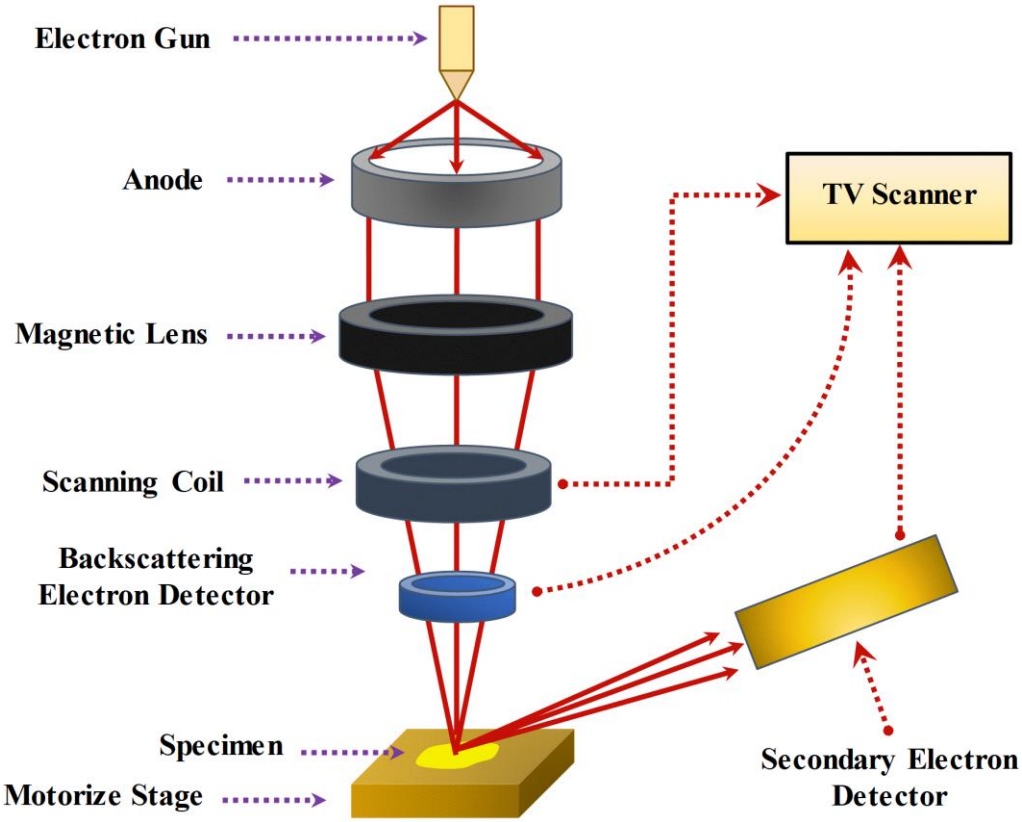

Figure 2.5 Schematic diagram of FESEM.

2.4.4 High-Resolution Transmission Electron Microscopy

TEM is a sophisticated characterization method for high-resolution imaging of thin samples [56]. It used the high energy electron beam to probe the sample. As the name suggests, it is a transmission mode method; therefore, it requires very thin films. The electron beam penetrates the films and makes an image on the fluorescent screen, and a magnified image is obtained [56]. For the thin films, ion beam milling and surface polishing are used to reduce the sample thickness to make it appropriate for the imaging. The time required for the sample preparation is longer. For the powder samples, the powder is dissolved in isopropanol or ethanol and ultra-sonicated to disperse it uniformly and deposited over copper mesh that is coated with the carbon from one side. This mesh

is used as a sample holder. Both crystalline and amorphous sample imaging is possible with this characterization. The HRTEM can resolve the atoms depending on the energy of the incident electron beam and the lenses. Along with the imaging, HRTEM can give the diffraction pattern of the localized particles [56].

2.4.5 Raman Spectroscopy

Raman spectroscopy stands as a robust spectroscopic technique for delving into the intricacies of phonons and molecular vibrations within materials [57]. This method uses the inelastic scattering of monochromatic light, typically derived from a laser beam. The photons from the laser light interact with the sample, inducing a shift in the frequency of the laser photons concerning the incoming monochromatic frequency. This phenomenon is termed the Raman shift that provides valuable insights into vibrational, rotational, and other low-frequency transitions within molecules. Such information is instrumental in identifying the chemical structure, phase, strain, and impurities present in the materials [57].

In the context of a solid material, the vibrational frequencies within the lattice are contingent upon the mass of the atoms and their respective bonds. The energy shift from the scattered photons is expressed as a change in frequency, denoted by the wavenumber shift ($\Delta\nu$). The mathematical representation is articulated as:

$$\Delta\nu = (\frac{1}{\lambda_1} - \frac{1}{\lambda_2})$$

Here, $\Delta\nu$ signifies the wavenumber shift, λ_1 represents the wavelength of the inelastic scattered photons, and λ_2 is the wavelength of the laser source. This equation quantifies the change in frequency resulting from the Raman scattering process.

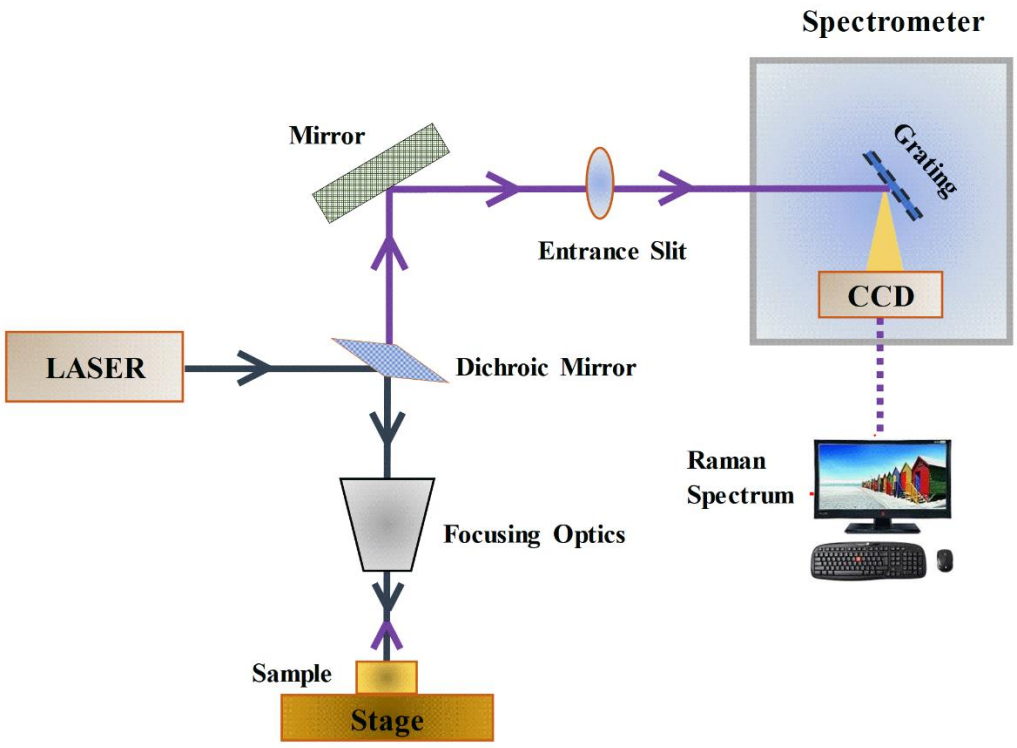

Figure 2.6 Schematic diagram of a dispersive Raman spectrometer setup.

The graphical representation in **Figure 2.6** elucidates how monochromatic light interacts with a material, leading to inelastic scattering and the subsequent Raman shift. In essence, Raman spectroscopy emerges as a sophisticated and insightful method for probing molecular vibrations and structures within materials.

2.4.6 Four-Probe Resistivity

The four-point probe method stands out as a straightforward and widely adopted approach for measuring the resistivity of samples. In this technique, four contacts are implanted on the surface of the thin film by applying silver glue. The two contacts positioned near the edges are linked to the power current supply, while the other two contacts are connected to a voltage meter. This arrangement allows for the passage of current through the outer

probes, inducing and measuring a voltage between the inner probes [58]. The resistance (R_{res}) of the region between the two inner probes is determined using Ohm's law:

$$R_{res} = \frac{V}{I}$$

The resistivity (ρ) can then be calculated using the formula:

$$\rho = \frac{Rres.d.Lw}{L}$$

Where, L represents the length between the two inner probes, L_w is the length of the contacts, and d is the thickness of the thin film. This equation provides a means to derive the resistivity of the thin film based on the measured resistance, dimensions, and contact length [58]. In the experimental setup, the film sample is affixed to a hot plate that connected to a temperature controller.

2.4.7 X-ray Photoelectron Spectrophotometer

XPS has been a non-destructive method to analyze the elemental composition with the charge state of the species of the sample's surface that can probe up to 1 nm. XPS is also called electron spectroscopy for chemical analysis (ESCA). If the XPS is used with the sputtering, it resolves the depth profiling of the sample [59]. The principle of the XPS is the photoelectric effect. The X-ray photon incident of the element ejects out the core electron from it, and then, by analyzing the kinetic energy and the intensity of these ejected electrons, the element and its charge state can be extracted [59]. The ejected electrons have been analyzed using the electron energy analyzer that separates them based on the kinetic energy of the electron. This kinetic energy is in relation to the binding energy of the orbital electrons. This binding energy is a fingerprint for the specific element and its ionic state. The resultant spectral lines are verified with the handbook of the XPS to define the ionic state of the elements along with its presence.

2.4.8 Scattering-Type Scanning Near-Field Optical Microscopy

Spectroscopic imaging with spatial resolution higher than the diffraction limit is possible using an s-SNOM. With the right light sources, s-SNOM has been essential to several nanoscale innovations. The diffraction limit of traditional far-field spectroscopy limits it to around half of the wavelength; however, s-SNOM provides a flexible, label-free method for nanoscale surface characterizations, which gets around this restriction [60, 61].

In s-SNOM, an AFM uses an intermittent contact mode or tapping mode with a sharp metallic tip to methodically scan the selected material. The tip apex is connected to an external light source (refer to **Figure 2.7**), and the dispersed light that results from the tip interacting with the sample is collected. An optical detector then converts this gathered light into an electric signal. The signal is routed to a lock-in amplifier, where the oscillation frequency of the tip is used as the reference frequency to separate non-fundamental harmonic demodulations [60, 61]. The external radiation's optical frequency is deliberately chosen to match the energy of a particular physical activity, including polaritonic, vibrational, or electronic resonances. A pseudo-heterodyne arrangement using a modified Michelson interferometer is shown in **Figure 2.7**. The tip is the focus of one interferometer arm, while an oscillating reference mirror is the target of the other. The near-field information of interest is captured in an interference signal that is produced when the reference beam interacts with the field that the tip scatters. The modulation frequencies of this signal are $n\Omega + mK$, where Ω and K stand for the oscillation frequencies of the probe and mirror, respectively. Nanoscale-resolved s-SNOM amplitude and phase pictures are obtained by using a lock-in amplifier to gather near-field amplitude and phase data as the tip scans the surface of the sample.

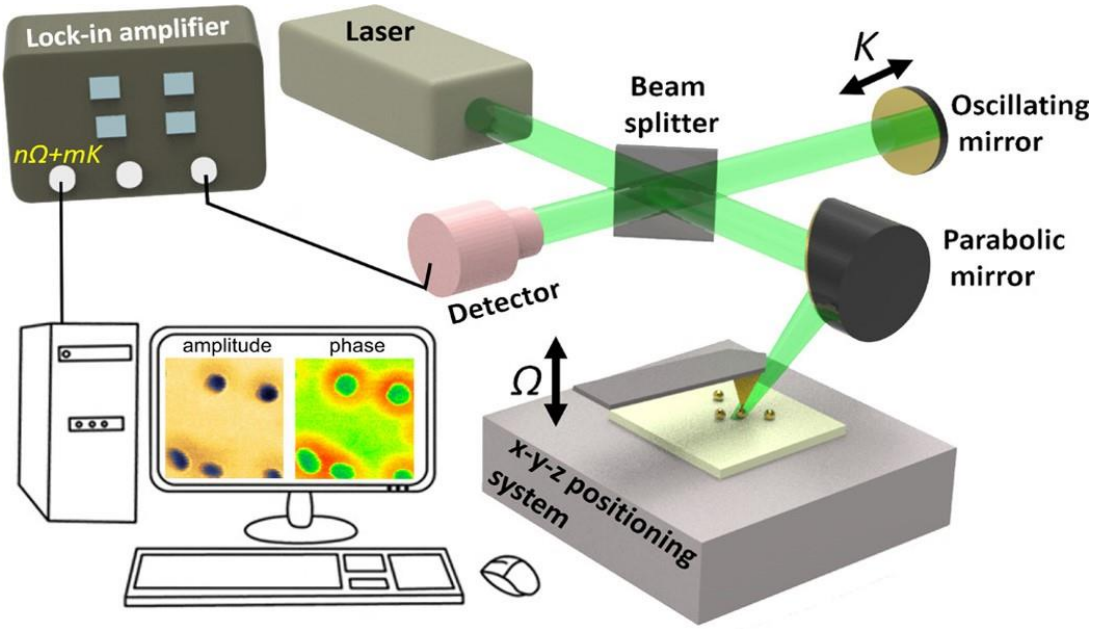

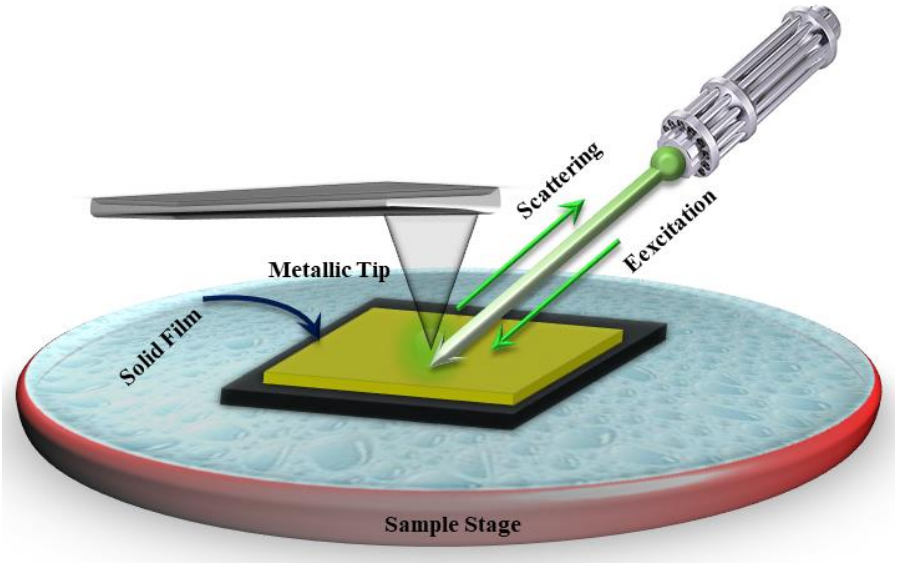

Figure 2.7 Diagram illustrating the setup of a s-SNOM imaging system functioning in a pseudo-heterodyne configuration and bottom image shows a close view of a tiny aperture illumination [62].

2.4.9 Impedance Spectroscopy

Electrical impedance quantifies a circuit's resistance to the flow of current. It is often represented as a complex number for mathematical convenience and is defined by:

$$Z = V/I$$

Here, V and I represent the voltage and current across the specimen. This concept is essentially an extension of Ohm's law, wherein the voltage and current are not restricted to real numbers but are expressed in complex form:

$$V = V_0 e^{i\omega t+\varphi_1}$$

$$I = I_0 e^{i\omega t+\varphi_2}$$

where V_0 = amplitude of voltage and I_0 = amplitudes of current, i = imaginary unit, ω = angular frequency of the electric excitation that relates with frequency f as $\omega = 2\pi f$, and φ is the phase.

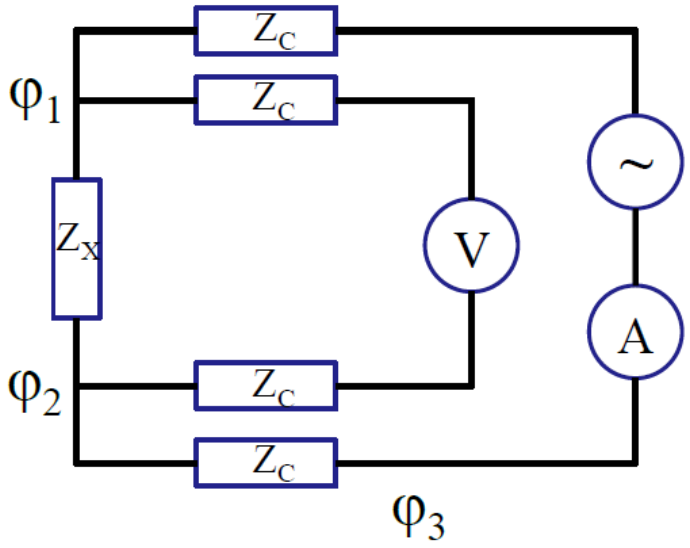

Figure 2.8 Circuit configuration for a four-point probe conducting impedance measurements.

Impedance spectroscopy (IS) is a testing technique employed to assess the frequency response of impedance (Z) for a specific circuit or sample [58]. The general circuitry for this method is depicted in **Figure 2.8.** The test outcomes are commonly visualized using a Nyquist plot, illustrating the real-imaginary curve of sample impedance, or a Bode plot, showcasing the frequency-dependent variations in both the magnitude and phase of sample impedance. To interpret and analyze impedance spectroscopy data, it is necessary to contemplate an equivalent circuit derived from an understanding of the sample's transport mechanism [58].

2.4.10 Semiconductor Device Analyzer

The electrical characterizations of the TFMs were studied in ambient atmospheric conditions using SC device analyzer with probe micro-manipulator to make the electrical contact with the TFMs. The I-V curve, or current-voltage (I-V) characteristic, is another name for it, depicts the correlation between the applied DC voltage and the resulting DC current through a sample. Typically, a variable voltage source is utilized to drive the sample, and the current is measured as the source varies across different voltage levels. The output characteristics are commonly used to ensure the TFMs operation, quality and its most critical device parameter such as V_{th}, ON/OFF ratio and hysteresis width and these properties describe the device non-linear and saturation behaviour.

REFRENCES

[1] I. A. Mogunov, S. Lysenko, A. E. Fedianin, F. E. Fernández, A. Rúa, A. J. Kent, A. V. Akimov, and A. M. Kalashnikova, "Large Non-Thermal Contribution to Picosecond Strain Pulse Generation Using the Photo-Induced Phase Transition in VO_2," *Nature Communication*s, **11** (2020) 1690 (8).

[2] R. Naik, B. D. Verma, and V. Balakrishnana, "Effect of Chemical Doping on Memristive Behaviour of VO_2 Microcrystals," *Applied Physics Letters*, **120** (2022) 062101 (6).

[3] G. Y. Song, C. Oh, S. Sinha, J. Son, and J. Heo, "Facile Phase Control of Multivalent Vanadium Oxide Thin Films (V_2O_5 and VO_2) by Atomic Layer Deposition and Postdeposition Annealing," *ACS Applied Materials and Interfaces*, **9** (2017) 23909–23917.

[4] S. Majid, D. K. Shukla, F. Rahman, S. Khan, K. Gautam, A. Ahad, S. Francoual, R. J. Choudhary, V. G. Sathe, and J. Strempfer, Insulator-Metal Transitions in the *T* phase Cr-Doped and *M*1 Phase Undoped VO_2 Thin Films," *Physical Review B*, **98** (2018) 075152 (9).

[5] M. Pattanayak, M. N. F. Hoque, Y. C. Ho, W. Li, Z. Fan, and A. A. Bernussi, "Ultrahigh Tunability of Resistive Switching in Strongly Correlated Functional Oxide," *Applied Materials Today*, **30** (2023) 101642 (11).

[6] J. S. Daubert, N. P. Lewis, H. N. Gotsch, J. Z. Mundy, D. N. Monroe, E. C., Dickey, M. D. Losego, and G. N. Parsons, "Effect of Meso and Micro-Porosity in Carbon Electrodes on Atomic Layer Deposition of Pseudocapacitive V_2O_5 for High Performance Supercapacitors," *Chemistry of Materials*, **27** (2015) 6524–6534.

[7] H. Yu, A. N. M. N. Islam, S. Mondal, A. Sengupta, and S. Ramanathan, "Switching Dynamics in Vanadium Dioxide-Based Stochastic Thermal Neurons," *IEEE Transactions on Electron Devices*, 69 (2022) 3135–3141.

[8] M. Pattanayak, M. N. F. Hoque, Y. C. Ho, W. Li, Z. Fan, and A. A. Bernussi, "Ultrahigh Tunability of Resistive Switching in Strongly Correlated Functional Oxide," *Applied Materials Today*, **30** (2023) 101642 (11).

[9] B. Hong, K. Hu, Z. Tao, J. Zhao, N. Pan, X. Wang, M. Lu, Y. Yang, Z. Luo, and C. Gao, "Polymorph Separation Induced by Angle Distortion and Electron Delocalization Effect via Orbital Modification in VO_2 Epitaxial Thin Films," *Physical Review B*, **95** (2017) 075433 (9).

[10] W. R. Mondal, E. Evlyukhin, S. A. Howard, G. J. Paez, H. Paik, D. G. Schlom, L. F. J. Piper, W. C. Lee, "Role of V-V Dimers on Structural, Electronic, Magnetic, and Vibrational Properties of VO_2 by First-Principles Simulations and Raman Spectroscopic Analysis," *Physical Review B*, **103** (2021) 214107 (13).

[11] N. Yuan, J. Li, and C. Lin, "Valence Reduction Process from Sol–Gel V_2O_5 to VO_2 Thin Films," *Applied Surface Science*, **191** (2002) 176–180.

[12] C. Zhang, W. Cao, A. V. Adedeji, and H. E. Elsayed-Ali, "Preparation and Properties of VO_2 Thin Films by a Novel Sol-Gel Process," *Journal of Sol-Gel Science and Technology*, **69** (2014) 320–324.

[13] A. Sharma, N. K. Chourasia, N. Pal, S. Biring, and B. N. Pal, "Role of Electron Donation of Tio_2 Gate Interface for Developing Solution-Processed High Performance One-Volt Metal-Oxide Thin-Film Transistor Using Ion-Conducting Gate Dielectric," *Journal of Physical Chemistry C*, **123** (2019) 20278–20286.

[14] P. V. Rajeswari, B. Tiwari, S. Ram, and D. Pradhan, "A Biogenic TiO_2-C-O Nanohybrid Grown from a Ti^{4+}-Polymer Complex in Green Tissues of Chilis, Interface Bonding, and Tailored Photocatalytic Properties," *Journal of Materials Science*, **53** (2018) 3131–3148.

[15] M. Saini, B. S. Dehiya, A. Umar, and M. S. Goyat, "Phase Modulation in Nanocrystalline Vanadium Di-Oxide (VO_2) Nanostructures Using Citric Acid via One Pot Hydrothermal Method," *Ceramic International*, **45** (2019) 18452–18461.

[16] A. Mishra, and S. Ram, "Surface Enhanced Optical Absorption and Photoluminescence in Nonbonding Electrons in Small Poly(Vinyl Pyrrolidone) Molecules," *Journal of Chemical Physics*, **126** (2007) 084902 (6).

[17] S. Ram, and H. J. Fecht, "Modulating up-Energy Transfer and Violet-Blue Light Emission in Gold Nanoparticles with Surface Adsorption of Poly(Vinyl Pyrrolidone) Molecules," *Journal of Physical Chemistry C*, **115** (2011) 7817–7828.

[18] Y. Gao, S. Wang, H. Luo, L. Dai, C. Cao, Y. Liu, Z. Chen, and M. Kanehira, "Enhanced Chemical Stability of VO_2 Nanoparticles by the Formation of SiO_2/VO_2 Core/Shell Structures and the Application to Transparent and Flexible VO_2-Based Composite Foils with Excellent Thermochromic Properties for Solar Heat Control," *Energy and Environmental Science*, **5** (2012) 6104–6110.

[19] Z. Tian, B. Xu, B. Hsu, L. Stan, Z. Yang, and Y. F. Mei, "Reconfigurable Vanadium Dioxide Nanomembranes and Microtubes with Controllable Phase Transition Temperatures," *Nano Letters*, **18** (2018) 3017−3023.

[20] D. Lee, J. Lee, K. Song, F. Xue, S. Choi, Y. Ma, J. Podkaminer, D. Liu, S. Liu, B. Chung, W. Fan, S. J. Cho, W. Zhou, J. Lee, L. Chen, S. H. Oh, Z. Ma, and C. Eom, "Sharpened VO_2 Phase Transition via Controlled Release of Epitaxial Strain," *Nano Letters*, **17** (2017) 5614−5619.

[21] S. N. Cassu, and M. I. Felisberti, "Poly(vinyl alcohol) and Poly(vinylpyrrolidone) Blends: 2. Study of Relaxations by Dynamic Mechanical Analysis," *Polymer*, **40** (1999) 4845−4851.

[22] S. Ding, Z. Liu, D. Li, W. Zhao, Y. Wang, D. Wan, and F. Huang, "Tunable Assembly of Vanadium Dioxide Nanoparticles to Create Porous Film for Energy-Saving Applications," *ACS Applied Materials and Interfaces*, **5** (2013) 1630–1635.

[23] M. Alsawafta, A. Almoabadi, S. Badilescu, and V. V. Truong, "Improved Electrochromic Properties of Vanadium Pentoxide Nanorods Prepared by Thermal Treatment of Sol-Gel Dip-Coated Thin Films," *Journal of Electrochemical Society*, **162** (2015) H466−H472.

[24] E. C. Nwanna, P. E. Imoisili, T. C. and Jen, "Fabrication and Synthesis of SnO_X Thin Films: a Review." *International Journal of Advanced Manufacturing Technology*, **111** (2020) 2809–2831.

[25] E. R. Costals, G. Masmitjà , E. Almache, B. Pusay, K. Tiwari, E. Saucedo, C. J. Raj, B. C. Kim, J. Piigdollers, I. Martin, C. Voz, and P. Ortega, "Atomic Layer Deposition of Vanadium Oxide Films for Crystalline Silicon Solar Cells," *Materials Advances,* **3** (2022) 337–345.

[26] J. A. Raiford, R. A. Belisle, K. A. Bush, R. Prasanna, A. F. Palmstrom, M. D. McGehee, and S. F. Bent, "Atomic Layer Deposition of Vanadium Oxide to Reduce Parasitic Absorption and Improve Stability in n–i–p Perovskite Solar Cells for Tandems," *Sustainable Energy and Fuels,* **3** (2019) 1517–1525.

[27] X. Yang, H. Xu, W. Liu, Q. Bi, L. Xu, J. Kang, M. N. Hedhili, B. Sun, X. Zhang, and S. D. Wolf, "Atomic Layer Deposition of Vanadium Oxide as Hole-Selective Contact for Crystalline Silicon Solar Cells," *Advanced Electronic Materials,* **6** (2020) 2000467 (8).

[28] E. C. Nwanna, R. A. M. Coetzee, and T. C. Jen, "Investigating the Purge Flow Rate in a Reactor Scale Simulation of an Atomic Layer Deposition Process," *American Society of Mechanical Engineers,* **59384** (2019) V02BT02A015.

[29] J. T. Cheung, "Pulsed Laser Deposition," *Handbook of Vacuum Science and Technology*, (1998) 694–710.

[30] J. Danglad-Flores, S. Eickelmann, and H. Riegler, "Deposition of Polymer Films by Spin Casting: A Quantitative Analysis," *Chemical Engineering Science*, **179** (2018) 257–264.

[31] M. F. Vostakola, S. M. Mirkazemi, and B. E. Yekta, "Structural, Morphological, and Optical Properties of W-Doped VO_2 Thin Films Prepared by Sol-Gel Spin Coating Method," *International Journal of Applied Ceramic Technology*, **16** (2019) 943–950.

[32] R. Liu, J. Wang, and Y. Song, "Polymer-Based Films for Artificial Intelligence," *Inorganic and Organic Thin Films: Fundamentals, Fabrication and Applications*, **2** (2021) 411–445.

[33] R. E. Marvel, K. Appavoo, B. K. Choi, J. Nag, and R. F. Hanglund Jr., "Electron-Beam Deposition of Vanadium Dioxide Thin Films," *Applied Physics A,* **111** (2013) 975–981.

[34] H. Yuce, H. Alaboz, Y. Demirhan, M Ozdemir, L. Ozyuzer, and G. Aygun, "Investigation of Electron Beam Lithography Effects on Metal-Insulator Transition Behavior of Vanadium Dioxide," *Physica Scripta*, **92** (2017) 114007 (8).

[35] A. Sarangan, G. Ariyawansa, I. Vitebskiy, and I. Anisimov, "Optical Switching Performance of Thermally Oxidized Vanadium Dioxide with an Integrated Thin Film Heater," *Optical Materials Express*, **11** (2021) 2348–2358.

[36] G. Tong, Y. Li, F. Wang, Y. Huang, B. Fang, X. Wang, H. Zhu, L. Li, Y. Shen, Q. Zheng, Q. Liang, M. Yan, Y. Qin, and J. Ding, "Thermal Oxidation-Grown Vanadium

Dioxide Thin Films on FTO (Fluorine-Doped Tin Oxide) Substrates," *Infrared Physics and Technology*, 61 (2013) 37–41.

[37] J. E. Greene, "Review Article: Tracing the Recorded History of Thin-Film Sputter Deposition: From the 1800s to 2017," *Journal of Vacuum Science & Technology A*, **35** (2017) 05C204 (60).

[38] N. Muslim, M. N. S. M. Idris, Y. W. Soon, Y. F. C. Chau, C. M. Lim, and N. Y. Voo, "Crystal Structure, Surface Topography, Surface Morphology and Optical Properties of Dc Magnetron Sputtered VO_2 Thin Films Using VO_2 Target," IOP Conference Series: Materials Science and Engineering, **409** (2018) 012025 (6).

[39] H. Zhang, J. S. Chernng, and Q. Chen, "Recent Progress on High Power Impulse Magnetron Sputtering (HiPIMS): The Challenges and Applications in Fabricating VO_2 Thin Film, *AIP Advances*, **9** (2019) 035242 (9).

[40] M. M. Seyfouri, and R. Binions, "Sol-Gel Approaches to Thermochromic Vanadium Dioxide Coating for Smart Glazing Application," *Solar Energy Materials and Solar Cells*, **159** (2017) 52–65.

[41] J. Livage, M. Henry, and C. Sanchez, "Sol-Gel Chemistry of Transition Metal Oxides," *Progress in Solid State Chemistry*, **18** (1988) 259–341.

[42] M. Wan, B. Liu, S. Wang, L. Hu, Y. He, H. Tao, and X. Zhao, "Optical Properties and Formation Mechanism of M1-Phase VO_2 Thin Films Annealed in a Closed NH_3 Atmosphere," *Journal of Alloys and Compounds*, **706** (2017) 289–296.

[43] C. B. Greenberg, "Undoped and Doped VO_2 Films Grown from $VO(OC_3H_7)_3$," *Thin Solid Films*, **110** (1983) 73–82.

[44] J. Du, Y. Gao, H. Luo, L. Kang, Z. Zhang, Z. Chen, and C. Cao, "Significant Changes in Phase-Transition Hysteresis for Ti-Doped VO_2 Films Prepared by Polymer-Assisted Deposition," *Solar Energy Materials and Solar Cells*, **95** (2011) 469–475.

[45] P. K. Ojha, R. Sharma, R. Hissariya, S. Babu, E. Ketkar, S. Singh, S. Neema, A. Rana, N. Pal, V. G. Sathe, and S. K. Mishra, "Observation of V-V Dimers Softening and Distinct Length Scales in Nanostructured VO_2 Thin Films," *Journal of Physics and Chemistry of Solids*, **163** (2022) 110564–110568.

[46] P. V. Rajeswari, S. K. Sharma, S. Ram, and D. Pradhan, "Nanoporous N/O:Sp^2-C Films Functionalized at Nonbonding Electrons of a Biogenic Husk (Green Chili) with Deep UV-Visible Light Absorption-Emission for Photocatalysis and other Applications," *Surfaces and Interfaces*, **38** (2023) 102824 (20).

[47] S. Jung, S. K. Sharma, and S. Ram, "A Metastable Cr^{4+}-Compound $AlCrO_{3+\delta}$, $\delta \leq 0.5$, Grown at a Nanocolloid, and Its Ultraviolet Absorption, Phonon Bands, and Dielectric Properties," *Journal of Alloys and Compounds*, **927** (2022) 166865 (11).

[48] A. Cvitkovic, N. Ocelic, and R. Hillenbrand, "Material-Specific Infrared Recognition of Single Sub-10 nm Particles by Substrate-Enhanced Scattering-Type Near-Field Microscopy," *Nano Letters*, **7** (2007) 3177–3181.

[49] C. McGahan, S. Gamage, J. Liang, B. Cross, R. E. Marvel, R. F. Haglund, and Y. Abate, "Geometric Constraints on Phase Coexistence in Vanadium Dioxide Single Crystals," *Nanotechnology*, **28** (2017) 085701 (9).

[50] H. T. Stinson, A. Sternbach, O. Najera, R. Jing, A. S. Mcleod, T. V. Slusar, A. Mueller, L. Anderegg, H. T. Kim, M. Rozenberg, and D. N. Basov, "Imaging the Nanoscale Phase Separation in Vanadium Dioxide Thin Films at Terahertz Frequencies," *Nature Communications*, **9** (2018) 3604 (9).

[51] Hu, C.; Li, L.; Wen, X.; Chen, Y.; Li, B.; Ren, H.; Zhao, S.; Zou, C. Manipulating the Anisotropic Phase Separation in Strained VO_2 Epitaxial Films by Nanoscale Ion-Implantation, *Appl. Phys. Lett.* **2021**, *119*, 121101 (6).

[52] B. Tiwari, S. Ram, and P. Banerji, "Biogenic Synthesis of Tunable Core-Shell C-$CaIn_2O_4$, Interface Bonding, Conductive Network Channels, and Tailored Dielectric Properties," *ACS Sustainable Chemistry and Engineering*, **6** (2018) 16298–16307.

[53] H. P. Klug, and L. E. Alexander, "X-Ray Diffraction Procedures: For Polycrystalline and Amorphous Materials," (1974).

[54] G. Binnig, C. F. Quate, and C. Gerber, "Atomic Force Microscope," *Physical Review Letters*, **56** (1986), 930–933.

[55] J. I. Goldstein, D. E. Newbury, J. R. Michael, N. W. M. Ritchie, J. H. J. Scott, and D. C. Joy, "Scanning Electron Microscopy and X-Ray Microanalysis," *Springer*, (2017).

[56] J. C. H. Spence, "High-Resolution Electron Microscopy," *OUP Oxford*, (2013).

[57] N. Colthup, "Introduction to Infrared and Raman Spectroscopy," *Elsevier*, (2012).

[58] Yuxia Ji, "Thermochromic VO_2-Based Materials for Smart Window," Ph.D. Thesis, *Uppsala University*, SE-751 21 Uppsala, Sweden, (2018).

[59] D. Briggs, M. P. Seah, "Practical Surface Analysis: by Auger and X-Ray Photo-Electron Spectorscopy," *Wiley*, (1983).

[60] L. Novotny, and B. Hecht, "Principles of Nano-Optics," *Cambridge University Press*, (2012).

[61] B. Knoll, and F. Keilmann, "Near-Field Probing of Vibrational Absorption for Chemical Microscopy," *Nature*, **399** (1999) 134–137.

[62] S. G. Stanciu, D. E. Tranca, G. Zampini, R. Hristu, G. A. Stanciu, X. Chen, M. Liu, H. A. Stenmark, and L. Latterini, "Scattering-Type Scanning Near-Field Optical Microscopy of Polymer-Coated Gold Nanoparticles," *ACS Omega*, **7** (2022) 11353–11362.